



Article

Spatial Characteristics of Global Strong Constant-Frequency Electromagnetic Disturbances from Electric-Field VLF Data of the CSES

Ying Han ^{1,*} , Qiao Wang ² , Jianping Huang ², Jing Yuan ¹, Zhong Li ¹ , Yali Wang ¹, Jingyi Jin ³ and Xuhui Shen ⁴

¹ Institute of Disaster Prevention, Sanhe 065421, China

² National Institute of Natural Hazards, Ministry of Emergency Management of China, Beijing 100085, China; qiaowang@ninhm.ac.cn (Q.W.); jianpinghuang@ninhm.ac.cn (J.H.)

³ College of Computer Science and Technology, Jilin University, Changchun 130012, China

⁴ National Space Science Center, Chinese Academy of Sciences, Beijing 100085, China

* Correspondence: hanying@cidp.edu.cn

Abstract: Ionospheric disturbances are mainly caused by solar and Earth surface activity. The electromagnetic data collected by the CSES (China Seismo-Electromagnetic Satellite, popularly known as the Zhangheng-1 satellite) can capture many space disturbances. Different spatial disturbances can exhibit distinctive shapes on spectrograms. Constant-frequency electromagnetic disturbances (CFEDs) such as artificially transmitted VLF radio waves, power line harmonics, and satellite platform disturbances can appear as horizontal lines on spectrograms. Therefore, we used computer vision and machine learning techniques to extract the frequency of global CFEDs and analyze their strong spatial signal characteristics. First, we obtained time-frequency spectrograms from CSES VLF electric-field waveform data using Fourier transform. Next, we employed an unsupervised clustering algorithm to automatically recognize CFED horizontal lines on spectrograms, merging horizontal lines from different spectrograms, to obtain the CFED horizontal-line frequency range. In the third stage, we verified the presence of CFEDs in power spectrograms, thus extracting their true frequency values. Finally, for strong CFED signals, we generated eight revisited periods, resulting in 10,230 power spectrograms for analyzing each CFED's spatial characteristics using a combined periodic sequence and spatial region that included frequency offsets, frequency fluctuations, and signal non-observation areas. These findings contribute to enhancing the quality of CSES observational data and provides a theoretical basis for constructing global CFED spatial background fields and earthquake monitoring and early prediction systems.

Keywords: China Seismo-Electromagnetic Satellite (CSES); constant-frequency electromagnetic disturbances (CFEDs); spectrogram; frequency extraction; spatial characteristics



Citation: Han, Y.; Wang, Q.; Huang, J.; Yuan, J.; Li, Z.; Wang, Y.; Jin, J.; Shen, X. Spatial Characteristics of Global Strong Constant-Frequency Electromagnetic Disturbances from Electric-Field VLF Data of the CSES. *Remote Sens.* **2023**, *15*, 3815. <https://doi.org/10.3390/rs15153815>

Academic Editor: Stephan Havemann

Received: 29 June 2023

Revised: 28 July 2023

Accepted: 28 July 2023

Published: 31 July 2023



Copyright: © 2023 by the authors. Licensee MDPI, Basel, Switzerland. This article is an open access article distributed under the terms and conditions of the Creative Commons Attribution (CC BY) license (<https://creativecommons.org/licenses/by/4.0/>).

1. Introduction

Since the 1980s, electromagnetic satellites have detected various spatial disturbances [1–7], including solar magnetic storms, substorms, lightning, atmospheric tides, artificial very-low-frequency (VLF) signals, power harmonics generated by power systems, and electromagnetic disturbances generated by satellite platforms themselves. These electromagnetic wave disturbances exhibit different shapes on spectrograms [8]. In order to meet the needs of navigation communication, ground-based VLF transmitting stations emit continuous electromagnetic waves at a constant frequency between 10 and 50 kHz. Due to their constant frequency, they are represented as a horizontal line on time-frequency diagrams [8]. The harmonic radiation generated by the ground power system is shown on spectrograms as several parallel lines that are significantly higher than the background intensity and are separated by 50/60 Hz [8,9], as shown in Figure 1. There is a weak current during the operation of the satellite in orbit,

generated by the solar cell panel receiving sunlight, providing power to the satellite payload. This current flow produces low-frequency magnetic-field disturbances [10], such as changes in the magnetic field observed by DEMETER's induction magnetometer—from 19.5 to 20 kHz in terms of power spectrum data [9]. Disturbance from DEMETER's own body occurs mainly in the frequency range of 1 to 8 kHz, with smaller disturbances occurring below 19.5 Hz, such as at frequencies 7.33 Hz, 19.53 Hz, 39.06 Hz, and their harmonics [11]. Current flows are generated when the solar wings on solar cell panels provide power, and these noises mainly manifest in the form of machine harmonics at frequencies of 8 Hz, 13.25 Hz, 31 Hz, 77 Hz, and their harmonics [12]. These constant-frequency electromagnetic disturbances (CFEDs) are presented as spectral horizontal lines on the spectrogram, which are higher than the background intensity level.

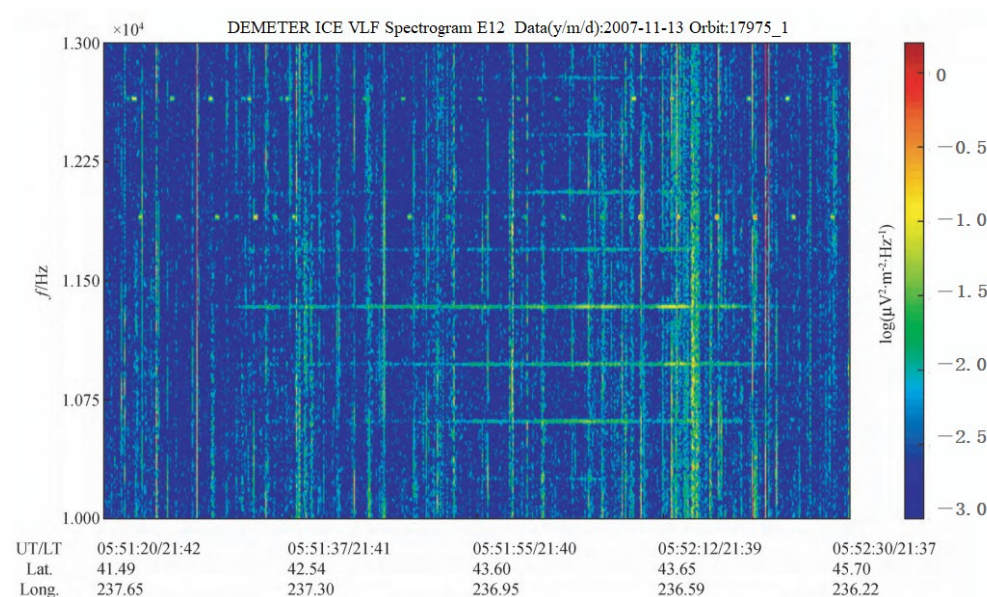


Figure 1. VLF spectrogram of an electric-field component recorded by the DEMETER satellite on 13 November 2007 in the frequency range 10–13 kHz. The y -axis represents frequency, the x -axis represents time, latitude, and longitude, and the color bar represents intensity.

Earthquakes are one of the most destructive natural disasters. Strong earthquakes often cause hundreds of thousands of deaths and property losses. A large number of studies have shown that electromagnetic anomalies are very sensitive to earthquakes [13–16]. When super-strong and shallow earthquakes occur, the energy of VLF and ultra-low-frequency (ULF) electromagnetic waves will become stronger, causing space ionospheric disturbances, which are used for short-term strong earthquake prediction [17,18]. One way to monitor ionospheric disturbances is to use VLF transmitters to transmit continuous VLF electromagnetic waves to space at different frequencies, which can penetrate the ionosphere. When the satellite flies over the transmitting station, the VLF signals are received synchronously by the satellite [19].

The main characteristics of VLF electromagnetic waves emitted from artificial source transmitters are low energy loss and long transmission distance. They can propagate over long distances between the Earth and the ionospheric waveguide system and exhibit significant wave–particle interaction effects [20–23]. When a satellite passes over an artificial source transmitter, it can receive the artificial source signal within a specific stable frequency range [24]. However, when electromagnetic waves propagate through the ionosphere, many parameters, including velocity and phase, as well as refraction and scattering effects, change. Therefore, the various electromagnetic responses that are excited by artificial source VLF signals in the ionosphere have different spatiotemporal characteristics [25]. There are more than 40 artificial-source VLF and low-frequency radio-wave transmitters worldwide, widely used for long-distance navigation, maritime navigation, underwater communication navigation, and ionospheric disturbance detection [26]. During the propagation process

of VLF/LF radio waves, anomalies are generated when the lower ionosphere above the propagation path is disturbed by various factors such as solar flares, magnetic storms, lightning discharges, and earthquakes.

The advancement of satellite detection technology has led to the utilization of electromagnetic-field detection as the primary scientific objective for exploring ionospheric environments. The identification of artificial VLF/LF signals from the ground is typically achieved through the use of electromagnetic detectors, which rely on probe potential detection and inductive magnetometers. Due to the proliferation of VLF/LF artificial transmitters worldwide, satellites can effectively record information at each station, serving as mobile spatial receiving stations that provide a platform for studying the detection of anomalous VLF/LF artificial source signals by satellites, including their use in seismic detection applications.

At present, the signal-to-interference-to-noise ratio (SNR) method is used for detecting satellite VLF radio wave signals to obtain earthquake-related disturbances. Studies have found that the SNR of the VLF radio wave signal decreases significantly before earthquakes, with recovery after the event and similar variations observed by multiple stations [27–33]. Similarly, the amplitude method used to detect satellite VLF wave signals can show a significant decrease or increase in the amplitude of the VLF wave signal before an earthquake [31–35]. Most of the current studies on electromagnetic response backgrounds are based on specific VLF transmitting stations and do not consider the global change characteristics of VLF constant-frequency electromagnetic disturbances (CFEDs) [36,37]. We attempt to utilize global CFEDs to study the anomalous changes before an earthquake. This necessitates an initial analysis and discussion of the spatial distribution characteristics of these CFEDs.

Therefore, this article uses CFED horizontal-line features on spectrograms [8,38] and integrates computer vision technology, unsupervised clustering methods, and statistical analysis. We have established a method for identifying CFEDs on time-frequency spectrograms, verifying and extracting their frequencies using power spectrograms. We then analyzed the spatial characteristics of each strong CFED using periodic sequences and spatial regions. This research provides a theoretical foundation for improving the quality of CSES observation data; studying and finding out what causes frequency fluctuation and frequency offset; investigating the characteristics of ionospheric anomalies potentially induced by earthquakes and the relationship between ionospheric disturbances and the occurrence of earthquakes; and targeting space-based earthquake monitoring and early warning systems.

2. Data Collection

On 2 February 2018, China launched its first satellite for the seismo-electromagnetic monitoring of the ionosphere over seismic-prone areas—the CSES (China Seismo-Electromagnetic Satellite, also known as the Zhangheng-1 satellite). Its goal is to obtain global electromagnetic field, ionospheric plasma, and high-energy particle observation data, to carry out real-time ionospheric dynamic monitoring and seismic-precursor tracking detection in China and surrounding areas, and to explore the mechanism of seismic ionospheric disturbance [39]. The CSES's scientific mission is to monitor the variations in the main parameters of the topside ionosphere (electric and magnetic fields, plasma parameters, charge particle fluxes) caused by natural emitters, especially earthquakes or those that are artificial [40].

The CSES carries eight types of scientific payloads [41,42]. The space electric-field detection is completed by the electric-field detector (EFD), which provides data application services for seismic observation research. The detection frequency bands are divided into: ULF (0–16 Hz), ELF (6 Hz–2.2 kHz), VLF (1.8 kHz–20 kHz), and HF (18 kHz–3.5 MHz). The CSES's full orbit is divided into ascending and descending orbits. The ascending orbit is from the south latitude to the north, and the descending orbit is from the north latitude to the south. There are 76 orbits in 1 revisited period, and the revisited period is 5 days. The flight time of each orbit is approximately 94.6 min [43]. The orbital spacing in one period is between 4.7° and 4.8° [44]. The working range is from 65° S to 65° N.

The data in this study are selected from the waveform data and power spectrum data of the Z components of the CSES electric-field VLF band. According to the CSES satellite data specification, the data structure is shown in Table 1.

First, waveform data of the Z component of the VLF electric field are converted from the time domain to the frequency domain using Fourier transform. Figure 2 shows the time-frequency spectrogram obtained by transforming the waveform data from descending orbit No. 051760.

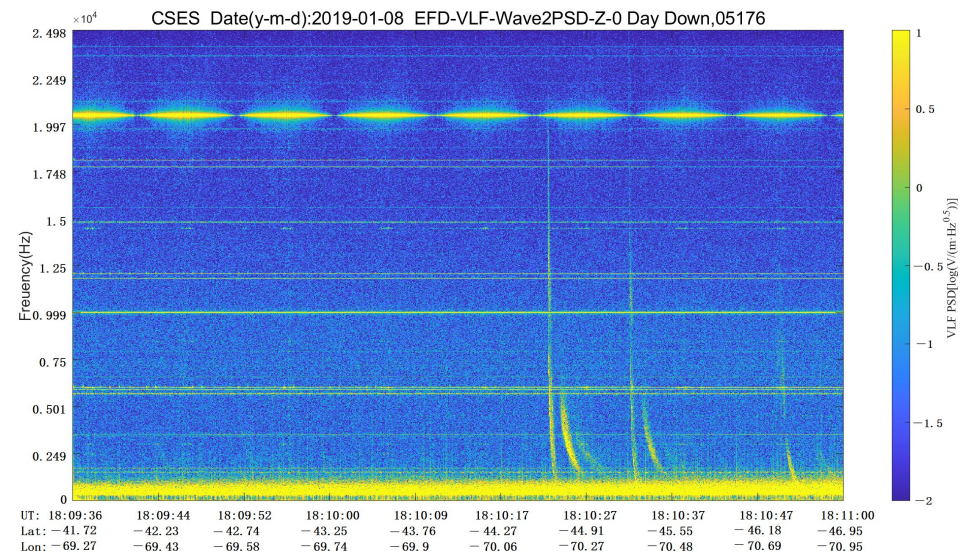


Figure 2. A time-frequency descending orbit spectrogram with No. 051760 on 8 January 2019 at 17:41–18:15. The y -axis is frequency, while the x -axis is time, latitude, and longitude. The color bar represents intensity. The horizontal lines on the figure depict various frequencies of CFEDs to be recognized.

Table 1. EFD VLF level 2 data-structure description.

Name	Content	Type	Size	Attribute	Remark
VERSE_TIME	Relative time	64-bit int	$N \times 1$	Unit: ms	
UTC_TIME	Absolute time	64-bit int	$N \times 1$	YYYYMMDD HHMMSSms	
WORKMODE	Work mode	16-bit int	$N \times 1$	1: Inspection 2: Detailed investigation -1: Invalid	
A131_W	X	64-bit float	$N \times 2048$	Unit: mV/m	X component of electric-field waveform in WGS84 coordinate system
A132_W	Y	64-bit float	$N \times 2048$	Unit: mV/m	Y component of electric-field waveform in WGS84 coordinate system
A133_W	Z	64-bit float	$N \times 2048$	Unit: mV/m	Z component of electric-field waveform in WGS84 coordinate system
A131_P	CH1	64-bit float	$N \times 1024$	Unit: mV/m/Hz ^{0.5}	Probe ab direction power spectrum
A132_P	CH2	64-bit float	$N \times 1024$	Unit: mV/m/Hz ^{0.5}	Probe cd direction power spectrum
A133_P	CH3	64-bit float	$N \times 1024$	Unit: mV/m/Hz ^{0.5}	Probe ad direction power spectrum
ALTITUDE	Satellite orbit height	32-bit float	$N \times 1$	Unit: km	The value in WGS84 spherical coordinate system
MAG_LAT	Geomagnetic latitude	32-bit float	$N \times 1$	Unit: degree	

Table 1. Cont.

Name	Content	Type	Size	Attribute	Remark
MAG_LON	Geomagnetic longitude	32-bit float	$N \times 1$	Unit: degree	
GEO_LAT	Geographical latitude	32-bit float	$N \times 1$	Unit: degree	The value in WGS84 spherical coordinate system
GEO_LON	Geographical longitude	32-bit float	$N \times 1$	Unit: degree	The value in WGS84 spherical coordinate system
FREQ	Power spectrum frequency	32-bit float	1024×1		
FLAG		32-bit int	$N \times 1$		Data Quality Label

3. Methodology

The study methodology consists of three main steps, as illustrated by the operational flowchart in Figure 3.

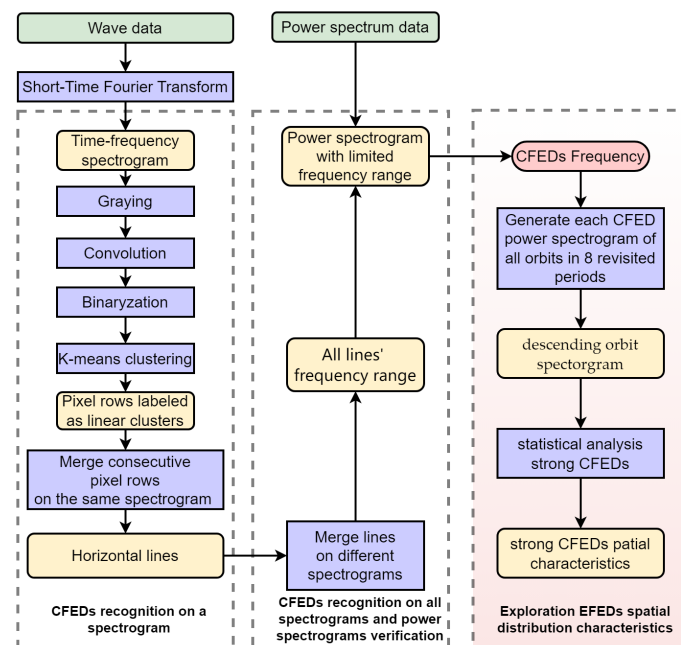


Figure 3. Flow chart of the entire work. This study is mainly in the third module: Exploration of the spatial distribution characteristics of CFEDs. In the figure, the green box represents the raw data collected by the CSES, the purple box represents various operations, the yellow box represents the intermediate data generated by various operations, the red elliptical box represents the data obtained for processing based on previous experiments in this paper, and the red gradient rectangular box represents the main process of this paper.

In the first stage, we recognize the horizontal lines generated by CFEDs on the time-frequency spectrogram and obtain the frequency range of CFEDs through the statistical analysis of a significant number of spectrograms.

In the second stage, using the frequency range obtained in the first step, we generate power spectrograms to validate the presence of CFEDs and automatically extract their actual frequencies.

In the third stage, we generate power spectrograms for multiple revisited orbital periods of each CFED. By analyzing the single orbital sequence and multiple revisited orbital periods in the same spatial domain, we aim to uncover the spatial characteristics of CFEDs.

3.1. CFEDs Automatic Recognition

CFEDs are represented as horizontal lines on the time-frequency spectrogram. The recognition of these lines is performed automatically using the following steps.

3.1.1. Graying

Since line recognition is based on the brightness relative to the background color, color information is unnecessary. To simplify the matrix and improve the computational speed, we first convert the spectrogram to grayscale. Grayscale conversion can be achieved using various methods, and in this study, we utilize the blue channel [45]. $\text{Gray} = \text{RGB} \cdot \text{B}$ represents the spectrogram, where RGB is the original spectrogram and B represents the blue channel. The grayscale result is shown in Figure 4b.

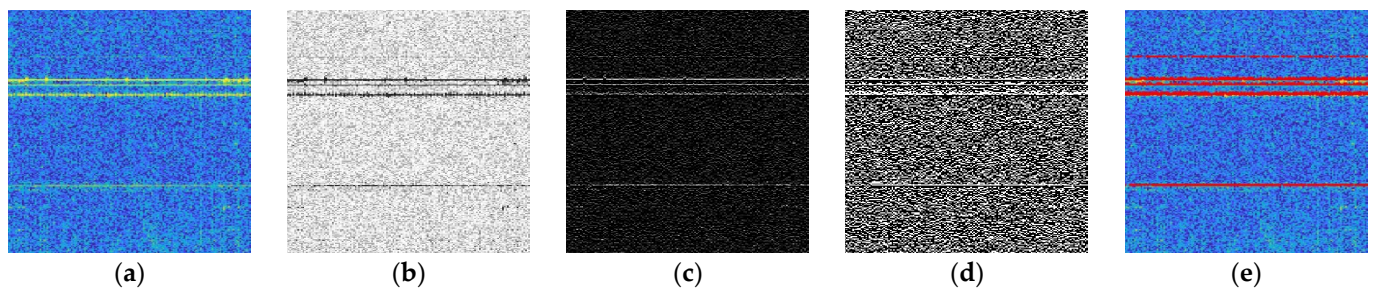


Figure 4. Presentation of the automatic process of horizontal-line recognition. (a) Original image; (b) Gray image; (c) Horizontal linear feature enhancement; (d) Binarization; (e) Lines recognized by red-dot marker.

3.1.2. Horizontal Feature Enhancement

To enhance the edge of horizontal lines and improve line recognition accuracy, we employ a horizontal convolution kernel [46]. The convolution kernel is described by Equation (1).

$$\text{kernel} = [1, 0, -1] \quad (1)$$

The convolution operation is performed as described in Equation (2), where Gray represents the grayscale spectrogram and Cov_dst represents the convolution result. The convolution result is shown in Figure 4c.

$$\text{cov_dst}(x, y) = \sum_{\substack{0 \leq x' < \text{kernel.cols}, \\ 0 \leq y' < \text{kernel.rows}}} \text{kernel}(x', y') \times \text{gray}(x + x' - \text{anchor.x}, y + y' - \text{anchor.y}) \quad (2)$$

3.1.3. Binarization

Binarization is used to convert each pixel into black or white, simplifying the image and helping the algorithm to accurately recognize lines. The binarization operation is described by Equation (3), where i and j represent pixel coordinates. In this experiment, we set $\text{max} = 255$ and $\text{tresh} = 10$. Figure 4d illustrates the binarization result.

$$\text{bi_map}(i, j) = \begin{cases} \text{max} & \text{if } \text{cov_dst}(i, j) > \text{tresh} \\ 0 & \text{otherwise} \end{cases} \quad (3)$$

3.1.4. K-Means Clustering

The K-means clustering algorithm is an unsupervised clustering analysis technique in machine learning. Initially, the data are divided into K groups, and K objects are randomly chosen as the initial clustering centers μ_j ($j = 1, 2, \dots, k$). The distance between each object $x^{(i)}$ and each seed clustering center μ_j is then calculated, and each object is assigned to

the nearest clustering center using Equation (4). The cluster center and assigned objects represent a cluster.

$$c^{(i)} := \operatorname{argmin}_j \|x^{(i)} - \mu_j\|^2 \quad (4)$$

For each assigned sample, the cluster center is recalculated according to Equation (5). This process is repeated until the termination condition is satisfied. In this study, K is set to 2 [45], enabling unsupervised clustering of the binary graph in both linear and nonlinear ways. The experiment was terminated after 10 iterations. Figure 4e shows the result of the line clustering, marked by red dots on the spectrogram.

$$\mu_i := \frac{\sum_{i=1}^m 1\{c^{(i)} = k\} x^{(i)}}{\sum_{i=1}^m 1\{c^{(i)} = j\}} \quad (5)$$

3.1.5. Calculation of Recognized Line Frequency

Calculating the recognized line frequency involves establishing a proportional relationship between the height of the time-frequency spectrogram and the frequency range. Figure 5 illustrates this relationship, and Equation (6) describes the column calculation. In this equation, $line_freq$ represents the CFED frequency corresponding to the recognized line, max_freq represents the maximum frequency depicted in the time-frequency spectrogram, map_height represents the height of the time-frequency spectrogram, and $line_height$ represents the height of the recognized line on the time-frequency spectrogram. When affected by other space electromagnetic waves, the line shape on the time-frequency spectrogram undergoes changes such as thinning, thickening, interruption, or even disappearance, due to signal coupling and background enhancement [28]. Therefore, while the line frequency does not accurately represent the real frequency, it approximates the actual value. To accurately recognize, merge, and extract the existence and frequency range of CFEDs corresponding to the line, a significant number of time-frequency spectrograms must be analyzed.

$$line_freq = max_fre - \frac{max_freq \times line_height}{map_height} \quad (6)$$

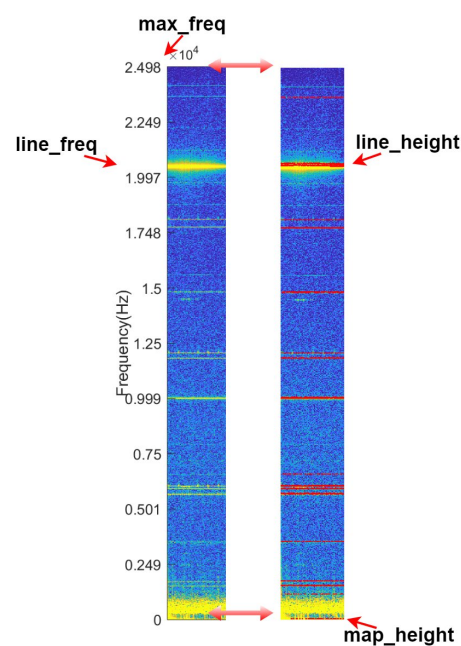


Figure 5. Demonstrates the correspondence between spectrogram height and frequency, with the red marker indicating the recognized line.

3.1.6. Combine the Lines to Determine the CFED Frequency Range

After recognizing lines on many spectrograms, each spectrogram has its own set of horizontal lines. Subtle changes in the shape of these lines result in different line frequencies. To determine whether the recognized lines on each spectrogram belong to the same CFEDs, lines with intersecting linear frequencies between any two spectrograms are merged using a union operation. Finally, all recognized lines on the spectrogram are merged in pairs using a merging algorithm to obtain the frequency range for each CFED.

3.2. Confirmed CFEDs and Extract Its True Frequencies

By performing the above operations, we obtain frequency ranges for many lines. However, these ranges do not represent the true frequency values of CFEDs. To confirm the existence of CFEDs within these ranges, we use power spectrograms. Using the power spectrum data, we generate 8 discontinuous revisited periods, totaling 10,230 power spectrograms, according to frequency ranges. These power spectrograms help us determine the presence and true frequency of CFEDs. Figure 6 illustrates one of the power spectrograms.

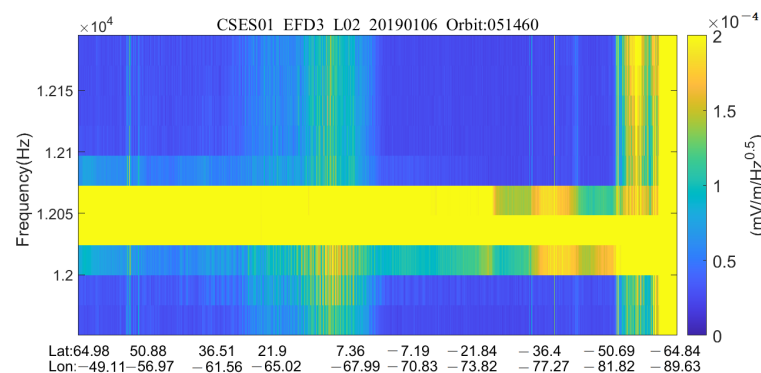


Figure 6. One of the frequency ranges (12.005 kHz, 12.207 kHz) is obtained by merging a large number of linear frequencies into different spectrograms. We use the frequency range (12.005 kHz, 12.207 kHz) to generate a power spectrogram on which there is a 12.05 kHz CFED. Note: In this paper, we use the approximate center value of a frequency domain to represent the CFED frequency.

3.3. CFED Spatial Characteristics Statistics

To analyze the spatial characteristics of CFEDs, we use the following methods.

Generate multiple revisited orbital-period CFED power spectrograms.

Perform statistical analyses of ascending and descending orbits to explore features and differences.

Analyze each CFED power spectrogram over a revisited orbital period to examine spectral variation characteristics.

Analyze CFED spatial distribution characteristics in the same spatial domain by examining multiple revisited orbital periods.

4. Experimental Results and Analysis

4.1. Experimental Environment

For this experiment, we used Matlab2020 to generate time-frequency and power spectrograms. We used the Cartopy library in Python 3.7 to draw geographic information and used CV2 and SKLearn libraries to recognize lines on time-frequency spectrograms.

4.2. Experimental Data

We randomly selected data from eight discontinuous revisited periods of CSES VLF data observed in 2019 and 2020. The data were preprocessed to retain only the full orbital period where the latitude range was (−64, 64) or (64, −64). Please refer to Table 2 for further details.

Table 2. Experimental data of eight discontinuous revisited periods.

Orbital Period	Start and End Time	The Time-Frequency Spectrogram Number	Descending Number	Ascending Number
Period 1	6 January 2019–10 January 2019	126	67	59
Period 2	20 July 2019–24 July 2019	126	65	61
Period 3	25 July 2019–29 July 2019	116	59	57
Period 4	30 July 2019–4 August 2019	142	74	68
Period 5	1 June 2020–5 June 2020	130	69	61
Period 6	26 June 2020–30 June 2020	131	69	62
Period 7	1 July 2020–5 July 2020	131	69	62
Period 8	22 July 2020–26 July 2020	121	62	59
	SUM	1023	534	489

4.3. Strong CFED Signals

A strong CFED signal is a clearly identifiable CFED on the power spectrogram. The CFED shown in Figure 7a is considered a strong CFED signal, while the one presented in Figure 7b requires careful identification. In this paper, we focus only on clearly identifiable CFEDs. We provide a detailed description of the spatial characteristics of 10 strong CFED signals in Section 4.5.5.

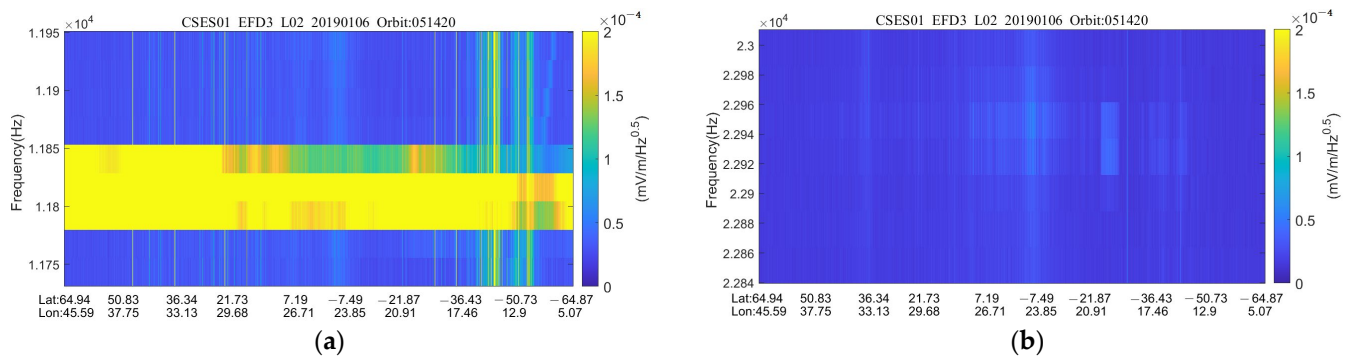


Figure 7. CFED power spectrograms. (a) Strong CFED signal at 11.8 kHz; (b) Weak CFED signal at 22.94 kHz.

4.4. Comparison of Ascending and Descending Signals

A complete orbit of the CSES includes ascending and descending orbits. The ascending orbit moves from the south to the north latitude, while the descending orbit moves from the north to the south latitude. Table 3 shows the power spectrograms of the ascending and descending orbits for four CFEDs over a revisited period. Through comparative analysis, we observe differences between the power spectrograms of ascending and descending orbits. There is too much interference in the power spectrum of the ascending orbit, which has a great influence on data analysis. Due to significant interference, the subsequent analysis is focused solely on descending orbits.

4.5. Spatial Characteristics of Strong CFEDs

Before analyzing the spatial characteristics of CFEDs, we provide two types of frequency variations: frequency fluctuation and frequency offset.

Frequency fluctuation: Within a single orbit's data spectrogram, the actual frequency of the CFED signal periodically increases or decreases relative to the expected frequency. Figure 8 shows examples of frequency fluctuations. In Figure 8a, the CFED with a frequency of 12.05 kHz exhibits frequency fluctuations in a latitude range of approximately (64.90, 15). Similarly, in Figure 8b, the CFED with a frequency of 18.1 kHz shows fluctuations in a latitude range of about (64.90, 15).

Table 3. Comparison of descending and ascending orbits.

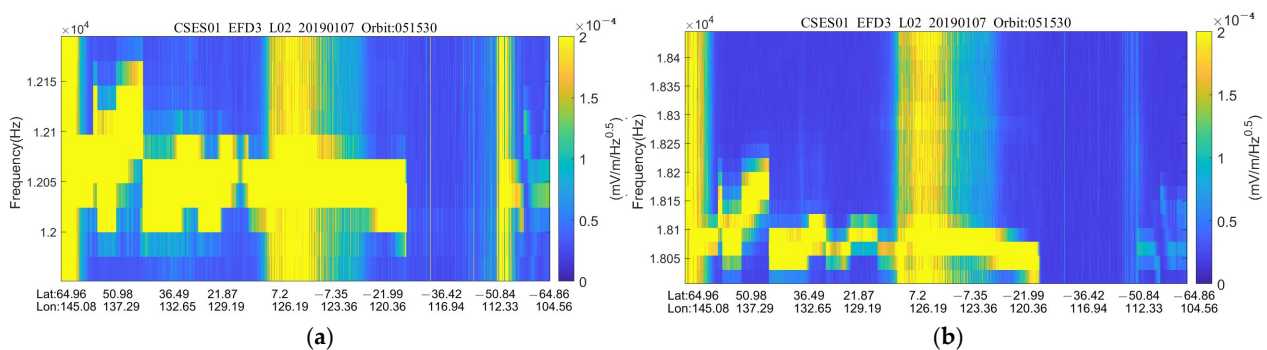


Figure 8. On the same orbit, CFEDs with different frequencies exhibit frequency fluctuations in the same spatial domain in one orbit data spectrogram. (a) CFED with a frequency of 12.05 kHz; (b) CFED with a frequency of 18.1 kHz.

Frequency offset: Frequency offset refers to the difference between the actual frequency of an electromagnetic wave and its expected or theoretical value. Figure 9 illustrates the

frequency offset within the same CFED (the same constant-frequency electromagnetic disturbance) and spatial domain. In Figure 9a, the CFED has a center frequency of about 11.80 kHz, while in Figure 9b, the CFED has a center frequency of about 11.85 kHz.

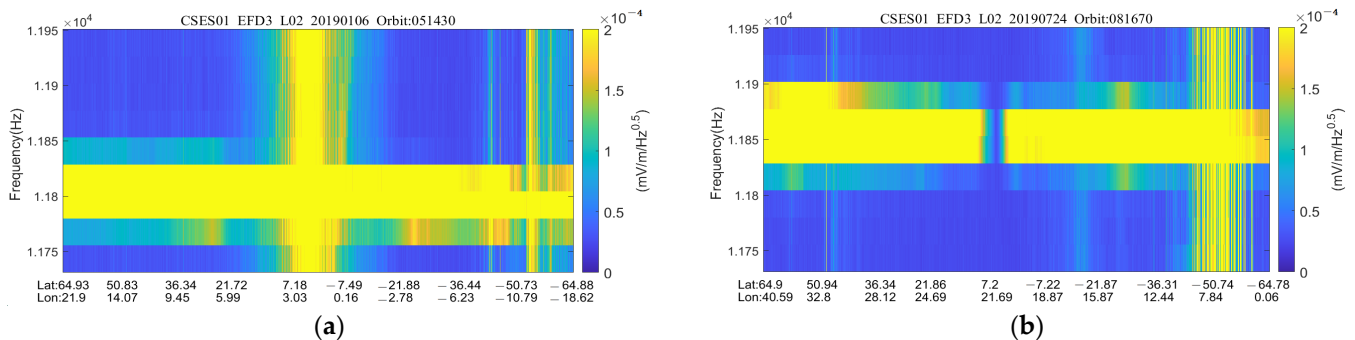


Figure 9. Frequency offset between spectrograms, the same spatial domain, the same CFED, but different frequencies. (a) CFED's center frequency is 11.8 kHz; (b) CFED's center frequency is 11.85 kHz.

Next, we delve into the spatial and frequency characteristics of strong CFEDs from various perspectives.

4.5.1. CFED with a Frequency of 12.05 kHz

This CFED, represented in Figure 10, exhibits strong characteristics with a frequency of 12.05 kHz.

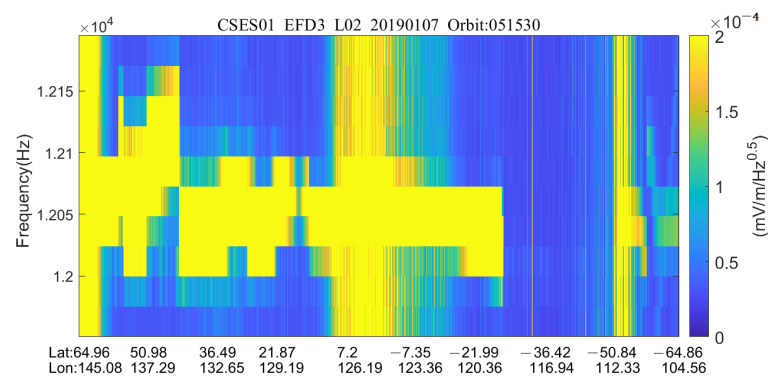


Figure 10. CFED with frequency of 12.05 kHz.

The CFED signal shows fluctuations within the descending orbit spectrogram, as shown in Figure 11.

Furthermore, Figure 12 shows the frequency offset between consecutive orbits of the same CFED in the same spatial domain, highlighting the changes in frequency.

In the identical spatial domain, the power spectrogram reveals consistent discontinuity characteristics for six revisited periods, as shown in Figure 13.

Figure 14 shows the approximate region, in descending orbits, where the 12.05 kHz CFED cannot be observed—at the latitude range of about $(-58, -22)$ and the longitude range of about $(31, 122)$.

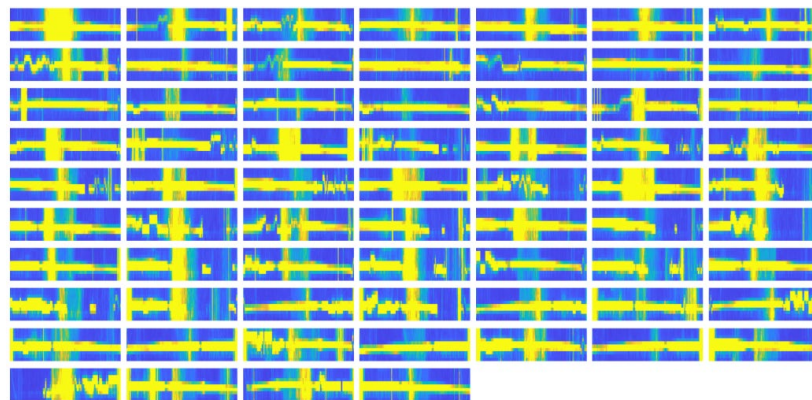


Figure 11. Illustrates the power spectrograms of the descending orbits for CFED at a frequency of 12.05 kHz during Period 1, showing frequency fluctuations.

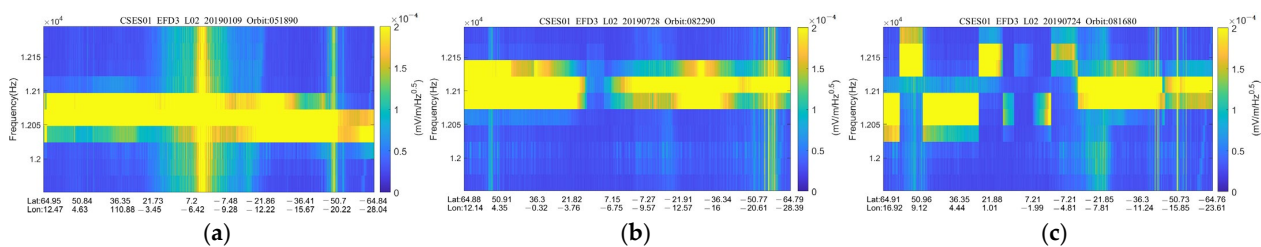


Figure 12. Frequency offset of three orbits of the same CFED. (a,b) are in the same spatial domain, but the central frequency values are different. (c) There is a change in the central frequency.

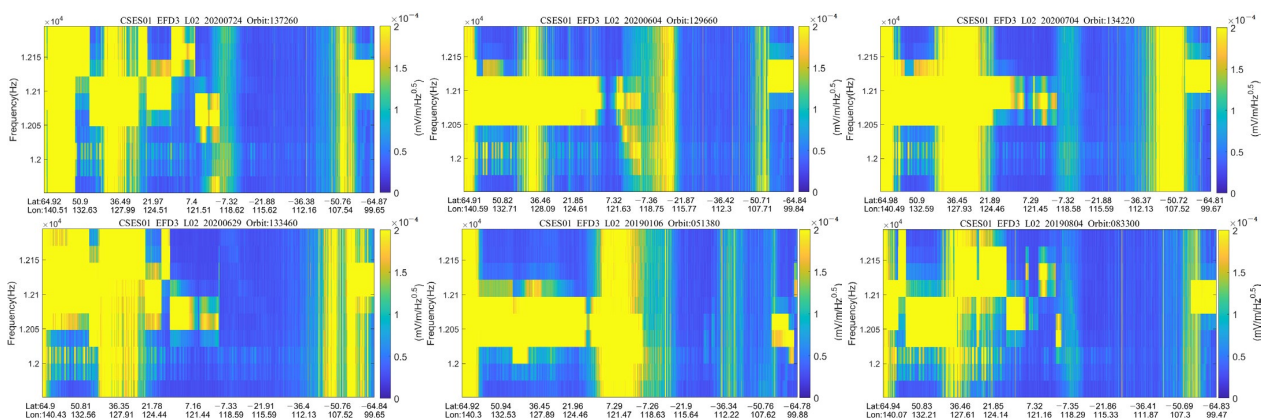


Figure 13. The same signal discontinuity characteristics of different orbits with the same longitude and latitude in the six revisited periods.

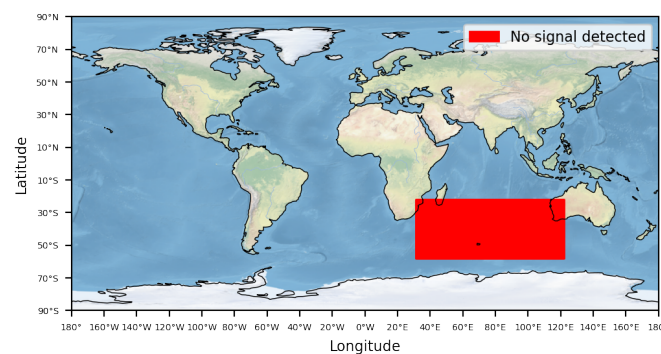


Figure 14. The approximate area of the 12.05 kHz CFED that cannot be observed by the descending orbits.

4.5.2. CFED with a Frequency of 10 kHz

The CFED signal with a frequency of 10 kHz is strong, as shown in Figure 15.

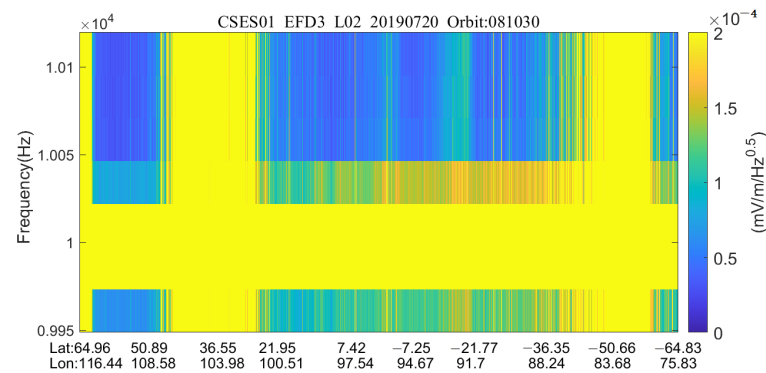


Figure 15. CFED with a frequency of 10 kHz.

This CFED exists throughout the orbit with a stable signal, characterized by no frequency offset, fluctuation, or discontinuity in certain areas, as shown in Figure 16.

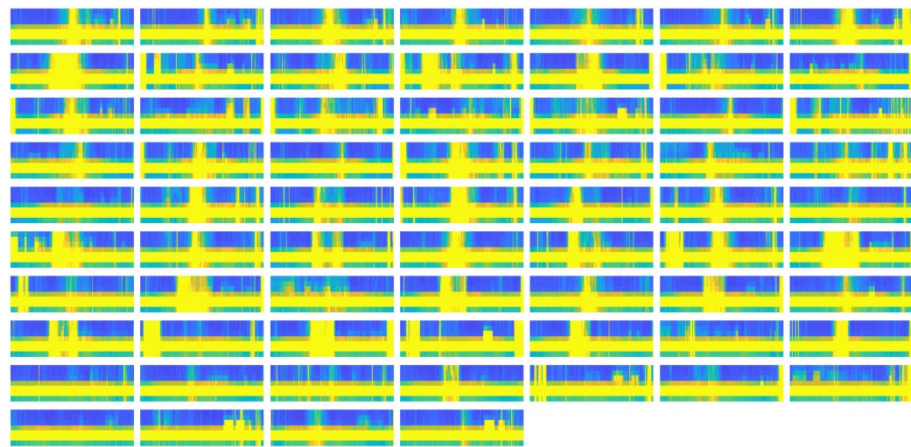


Figure 16. 10 kHz CFED descending orbit power spectrograms of Period 1. The signal is very stable.

4.5.3. CFED with Frequencies of 6.05, 5.95 kHz

This CFED consists of two frequencies that coexist or undergo simultaneous discontinuity in the spectrogram, as shown in Figure 17.

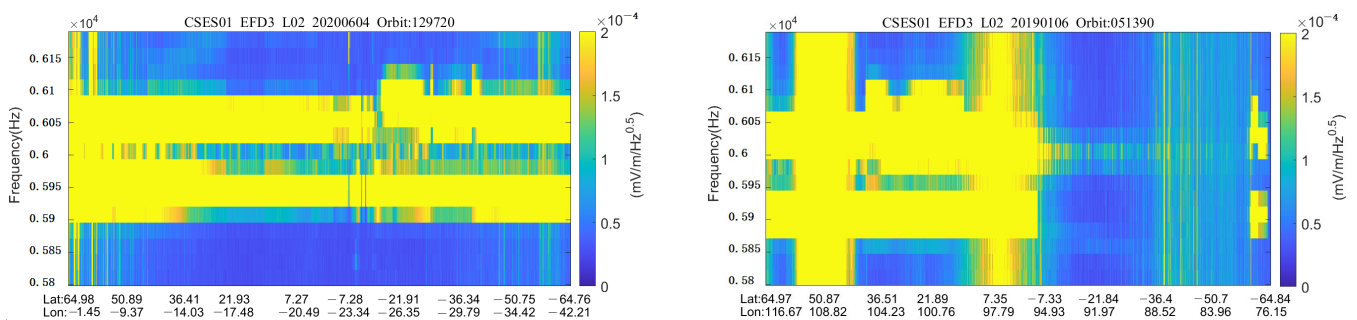


Figure 17. Two spectrograms of CFED with frequency of 6.05, 5.95 kHz.

Minor frequency fluctuations are observed in the descending orbit power spectrograms, as shown in Figure 18.

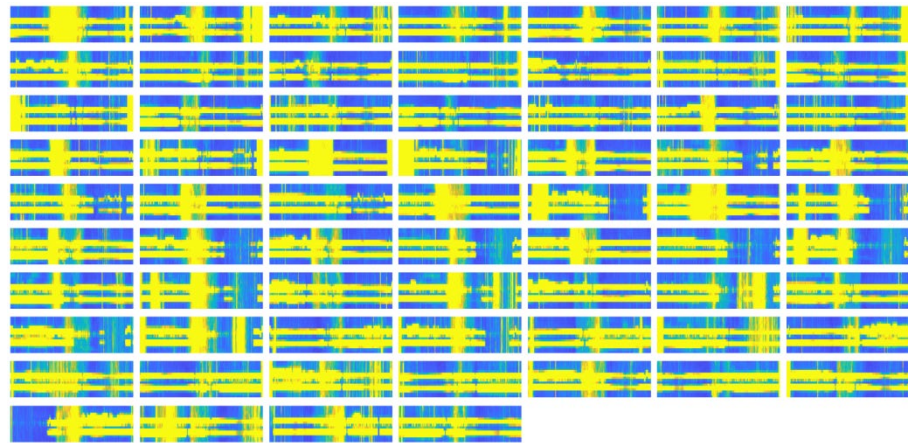


Figure 18. Descending orbit power spectrograms of Period 1 with a small frequency fluctuation.

Figure 19 shows the frequency offset between two orbits of the same CFED in the same spatial domain.

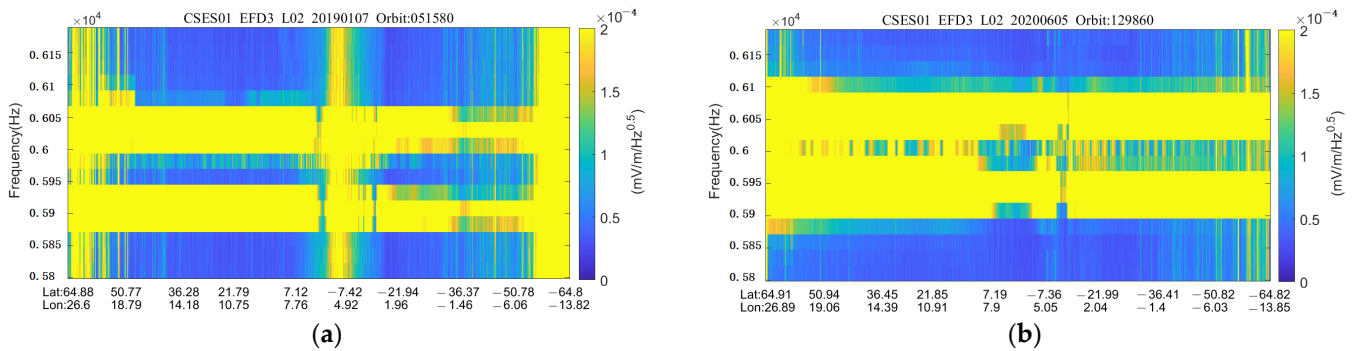


Figure 19. Frequency offset of two orbits of the same CFED. (a,b) are in the same spatial domain.

The spectrogram in Figure 20 shows consistent discontinuity characteristics for six revisited periods in the same latitude and longitude spatial domain.

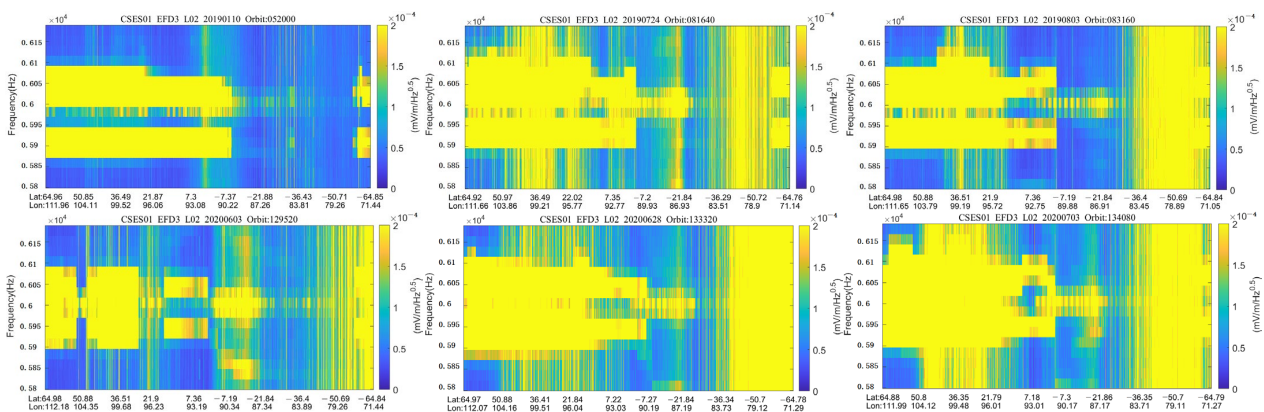


Figure 20. The same signal discontinuity characteristics of different orbits with the same longitude and latitude in the six revisited periods.

Similar to the previous CFED, Figure 21 shows regions in the descending orbits where CFEDs with frequencies of 6.05 kHz and 5.95 kHz cannot be observed, specifically the latitude range (−58, −22) and longitude range (31, 122).

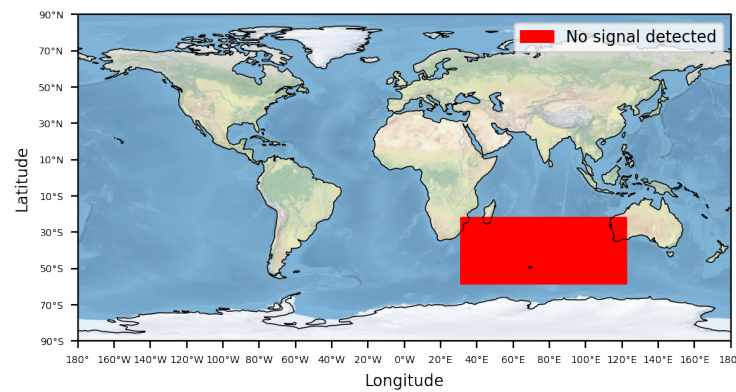


Figure 21. The approximate area of the 6.05, 5.95 kHz CFED that cannot be observed by the descending orbits.

4.5.4. CFED with a Frequency of 20.5 kHz

The CFED signal with a frequency of 20.5 kHz appears strong, as shown in Figure 22.

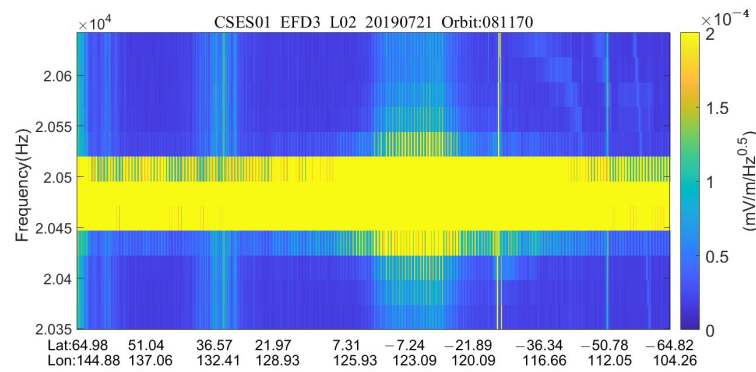


Figure 22. CFED with a frequency of 20.5kHz.

This CFED exists throughout the orbit with a stable signal, characterized by no frequency fluctuation, offset, or discontinuity in certain areas, as shown in Figure 23.

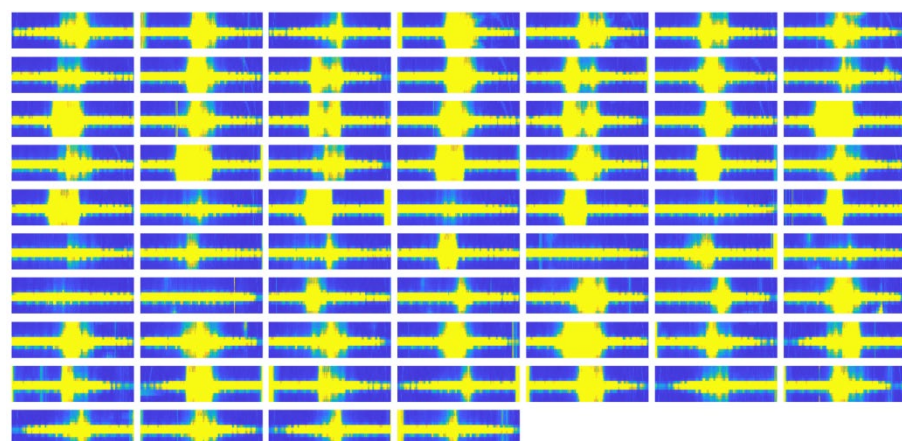


Figure 23. 20.5 kHz CFED descending orbit power spectrograms of Period 1. The signal is very stable.

The four CFEDs mentioned above are analyzed in detail, while the others including the four above are summarized in Table 4.

Table 4. Spatial characteristics of strong CFEDs.

Frequency kHz	Spectrogram	Descending Orbit Power Spectrograms of Period 1	Fluctuation	Off Set	Discontinuity	Unobserved Areas
12.05			Yes	Yes	Yes	Lat (-58, -22) Lon (31, 122)
10			No	No	No	No
6.05 5.95			Yes	Yes	Yes	Lat (-58, -22) Lon (31, 122)
20.5			No	No	No	No

Table 4. Cont.

Frequency kHz	Spectrogram	Descending Orbit Power Spectrograms of Period 1	Fluctuation	Off Set	Discontinuity	Unobserved Areas
15.58			No	No	No	No
14.5			No	No	No	No
18.1			Yes	Yes	Yes	Lat (-58, 0) Lon (34, 130)
11.8			No	Yes	Yes	Lat (-50, -36) Lon (117, 122); Lat (-58, -22) Lon (104, 120); Lat (-58, 0) Lon (71, 120); Lat (-58, -22) Lon (38, 78)

Table 4. Cont.

Frequency kHz	Spectrogram	Descending Orbit Power Spectrograms of Period 1	Fluctuation	Off Set	Discontinuity	Unobserved Areas
17.7			No	Yes	Yes	Lat (-58, -22) Lon (33, 119)
23.7			No	Yes	Yes	Lat (-50, -36) Lon (117, 122); Lat (-58, -22) Lon (104, 120); Lat (-58, 0) Lon (71, 120); Lat (-58, -22) Lon (38, 78)

4.5.5. Show Strong CFEDs in Table

Table 4 summarizes the spatial characteristics of ten strong CFEDs, including the four previously discussed CFEDs. The table provides information on frequency fluctuations, offsets, signal discontinuity, and unobserved areas for each CFED. Lat represents latitude, Lon represents longitude.

Through experimental analysis and statistics, we observe that these strong CFEDs possess distinct spatial characteristics. Some are present throughout the period orbits, while others exhibit frequency fluctuations or offsets and cannot be observed in specific areas. However, they also share common characteristics. CFEDs with frequency offsets tend to be unobserved in certain spatial domains. These unobserved areas are mainly concentrated in the southeastern hemisphere, as shown in Figure 24. Further discussion is needed to explore the shared and distinctive characteristics of these strong CFEDs.

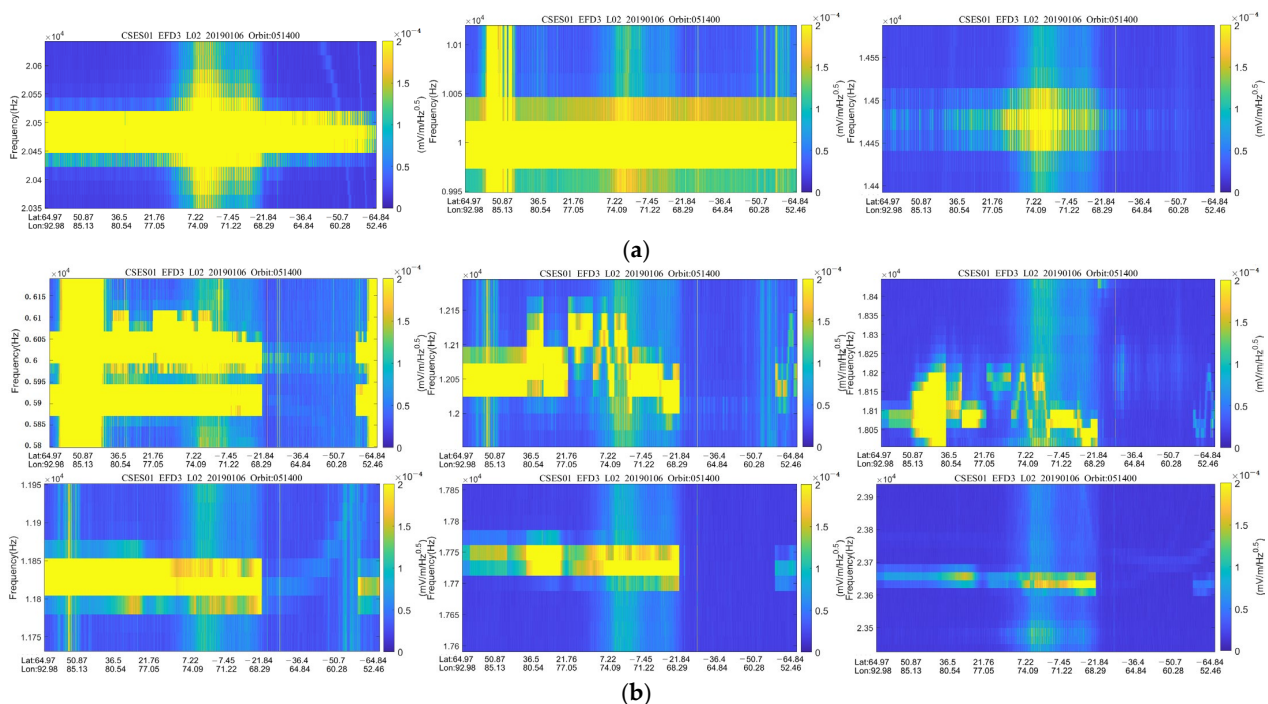


Figure 24. Nine strong CFEDs observed on the same orbit (051400). In (a), three strong CFEDs exhibit stable signals, while in (b), six CFEDs display instability due to frequency offset over time. These six CFEDs are mostly unobserved or are discontinuous within the same spatial domain.

5. Discussion

In this paper, regarding the horizontal-line characteristics of CFEDs in spectrograms, we used computer vision techniques to recognize these lines and extracted the corresponding CFED frequency values. The statistical analysis of the spatiotemporal characteristics of global strong CFED events revealed the presence of frequency offsets, frequency fluctuations, and data differences between ascending and descending orbits observed on the CSES. Aiming at these spatiotemporal characteristics of CFEDs, we will now proceed to discuss each of them separately.

5.1. Frequency Offset

Frequency offset is the difference between the actual frequency of a signal and the expected frequency. During signal generation or transmission, various disturbances or errors can cause the actual frequency to deviate from the set or expected frequency [47]. There are many reasons for frequency offset, such as temperature changes that can alter the physical characteristics of electronic components and circuits, leading to frequency

offset [48]. Over time, electronic components and circuits can be affected by aging and degradation, resulting in frequency drift [49]. Issues with the quality and stability of the power supply can cause frequency offset [50]. Environmental conditions such as humidity, air pressure, and altitude can also affect the performance of electronic devices and circuits, leading to frequency offset [51], among other factors.

Frequency offset can lead to a decrease in communication quality, signal distortion, increased error rate, data loss, and damage. It has a significant impact on the correct reception, decoding, and processing of signals [52–55]. Therefore, studying and understanding the characteristics and causes of frequency offset is crucial for effective signal transmission and processing. Based on the statistical analysis of the experiments mentioned above, several strong carrier-frequency-estimation devices exhibit noticeable frequency offsets.

In this paper, these CFEDs include 12.05 kHz, 6.05–5.95 kHz, 18.1 kHz, 11.8 kHz, 17.7 kHz, 23.7 kHz, etc. (We use the approximate center value of the frequency to represent a CFED). These frequency offsets have a significant impact on the quality of data analysis. Therefore, future research is needed to investigate the causes of these frequency offsets and explore methods to reduce them.

However, frequency offset quantification analysis can also be used to detect and monitor the stability and consistency of electromagnetic waves, as well as for applications such as spectrum analysis and signal processing. When studying earthquake precursors or other related phenomena, the occurrence of frequency offset may indicate changes or abnormal conditions in the electromagnetic-wave propagation environment [56–60]. Future research can be conducted based on the phenomenon of frequency offset to explore phenomena related to earthquake precursors.

5.2. Frequency Fluctuation

Frequency fluctuation is the periodic increase or decrease in the actual frequency of a signal relative to the expected frequency over a certain period of time [61]. Frequency fluctuations can be observed and quantified by the frequency-spectrum analysis of the signal. There can be various reasons for frequency fluctuations. For example, temperature variations can cause changes in the physical characteristics of electronic components and circuits, leading to frequency fluctuations [62]. Over time, the aging and degradation of electronic components and circuits can also cause frequency fluctuations [63]. Quality and stability issues in the power supply can lead to frequency fluctuations [64]. Environmental conditions such as humidity, air pressure, and altitude can affect the performance of electronic devices and circuits, leading to frequency fluctuations [65].

Frequency fluctuations can cause a decrease in communication quality, signal distortion, increased error rates, as well as data loss and corruption [66–69]. However, frequency fluctuations also have significance. For example, they can be used to monitor and analyze the propagation characteristics and environmental changes of electromagnetic waves, which is important for communication networks, radar systems, and more [70]. More importantly, the occurrence of frequency fluctuations can indicate the possibility of earthquake precursors or other related phenomena, providing important clues for earthquake research [71]. Signal-processing and frequency-spectrum analysis: by processing and analyzing frequency fluctuations, useful information can be extracted from the signal and used for frequency-spectrum analysis and signal-processing applications [72].

In this experiment, we observed frequency fluctuations in several CFEDs on the CSES (Chinese Seismo-Electromagnetic Satellite), such as 12.05 kHz, 6.05–5.95 kHz, and 18.1kHz, etc. Our future work will focus on investigating the causes of these CFEDs' frequency fluctuations, as well as further studying the extent and temporal-spatial domains of fluctuations to prepare for seismic-precursor prediction research.

5.3. Data Difference between Ascending and Descending Orbits on the CSES

Based on experimental statistics and analysis, we found that there are some differences in the quality of ascending and descending orbital data from the CSES satellite. These

differences manifest themselves as clearer, and there is less background disturbance in power spectrograms generated during descending orbits compared to ascending orbits. One of the reasons for the differences between ascending and descending orbit data is due to their different orbital positions and inclinations, which result in changes in the related physical environment and observation conditions [73,74]. Satellites ascend from lower orbital altitudes to higher ones during ascending orbits, while they descend from higher altitudes to lower ones during descending orbits, leading to different physical conditions in different altitude ranges. Secondly, the ascending and descending orbits pass through different times and locations on Earth, resulting in the observation of different physical phenomena and environmental conditions at different times, thereby causing differences in the data between ascending and descending orbits [75,76].

To address the differences in ascending and descending orbit data, it is common to treat them as separate data sets, allowing for a better understanding and interpretation of the characteristics and trends within each data set [77,78]. Additionally, based on factors such as orbital altitude and local time, segment analysis or specific analysis methods can be employed for the ascending orbit data [79,80]. In summary, when dealing with satellite ascending and descending orbit data, it is important to recognize their differences and employ appropriate data analysis and processing methods to fully understand and utilize the characteristics and information within these two data sets.

5.4. Method Improvement

At present, we use artificial statistical methods to process data, but as the amount of data increases, this operation is not accurate enough, and the workload is very large. The next stage of work, based on computer vision technology, uses machine learning methods to automatically identify CFEDs on the power spectrogram and accurately calculate the discontinuity area. Data accuracy is very important for clearing waveform data or background fields.

In addition, we only processed 10 strong CFEDs signals. Using machine learning methods, we can improve the ability of data processing not only for weak CFED signals but also for CFEDs with a small geographical coverage.

6. Conclusions

Seismic ionospheric disturbances exhibit complex and diverse characteristics. To enhance the early prediction of earthquakes using CSES satellite observation data, it is essential to understand the spatial and temporal distribution of other electromagnetic disturbances. Therefore, we used computer vision technology to extract the frequency ranges of global CFEDs from time-frequency spectrograms obtained by the Fourier transformation of waveform data. By analyzing a dataset of 1023 full-orbit waveform samples and 10,230 strong CFED power spectrograms captured during 8 revisited CSES EFD VLF periods, we identified their spatial characteristics in both ascending and descending orbits, including frequency fluctuations, frequency offsets, and unobserved areas. Through this analysis, we discovered both shared and distinctive spatiotemporal features among these CFEDs. These findings contribute to enhancing the quality of CSES observational data. In addition, they hold significant value for studying the disturbance characteristics of other space electromagnetic waves, earthquake monitoring, early prediction efforts, and waveform data cleaning through waveform suppression.

Moving forward, our research will focus on three main aspects: investigating the factors contributing to these spatial features; exploring patterns of change in CFEDs and other spatial disturbances—in particular, the variation in CFEDs before earthquakes; and implementing CFED-suppression techniques to clean waveform data.

Author Contributions: Conceptualization, methodology, writing—original draft, and writing—review and editing, Y.H.; methodology, Q.W. and J.Y.; data curation, J.H.; supervision, X.S.; and investigation, resources, and software, Z.L., Y.W. and J.J. All authors have read and agreed to the published version of the manuscript.

Funding: This research was funded by Education Research and Teaching Reform of Institute of Disaster Prevention Technology (No. JY2023B42), Fundamental Research Funds for the Central Universities (No. ZY20215143), NSFC project (No. 42104159), Teacher Research Fund Project (No. 20150109), Investigation of the Lithosphere Atmosphere Ionosphere Coupling (LAIC) Mechanism before the Natural Hazards, and Open Project Fund of Hebei Key Laboratory of Seismic Disaster Instrument and Monitoring Technology (No. FZ224104).

Data Availability Statement: Publicly available datasets were analyzed in this study. The CSES electric-field data can be found here: (www.leos.ac.cn, accessed on 1 September 2022).

Acknowledgments: This work used the data from the CSES mission, a project funded by the China National Space Administration (CNSA) and the China Earthquake Administration (CEA). Thanks to the CSES team for the data (www.leos.ac.cn, accessed on 1 September 2022). And acknowledge the International Space Science Institute (ISSI in Bern, Switzerland, and ISSI-BJ in Beijing, China) for supporting International Team 23-583 lead by Dedalo Marchetti and Essam Ghamry.

Conflicts of Interest: The authors declare no conflict of interest.

References

1. Yan, R.; Shen, X.; Huang, J.; Wang, Q.; Chu, W.; Liu, D.; Yang, Y.; Lu, H.; Xu, S. Examples of unusual ionospheric observations by the CSES prior to earthquakes. *Earth Planet. Phys.* **2018**, *2*, 79–90. [[CrossRef](#)]
2. Larkina, V.I.; Nalivaiko, A.V.; Gershenson, N.I.; Gokhberg, M.B.; Liperovskii, V.A.; Shalimov, S.L. Intercosmos-19 observations of VLF emissions associated with seismic activity. *Geomagn. Aeron.* **1983**, *23*, 842–846.
3. Chmyrev, V.M.; Isaev, N.V.; Bilichenko, S.V.; Stanev, G. Observation by space-borne detectors of electric fields and hydromagnetic waves in the ionosphere over an earthquake center. *Phys. Earth Planet. Inter.* **1989**, *57*, 110–114. [[CrossRef](#)]
4. Parrot, M.; Mogilevsky, M. VLF emissions associated with earthquakes and observed in the ionosphere and magnetosphere. *Phys. Earth Planet. Inter.* **1989**, *57*, 86–99. [[CrossRef](#)]
5. Pulnits, S.A.; Legen'ka, A.D. Spatial–Temporal Characteristics of Large Scale Disturbances of Electron Density Observed in the Ionospheric F-Region before Strong earthquakes. *Cosm. Res.* **2003**, *41*, 221–230. [[CrossRef](#)]
6. Liu, Y.M.; Wang, J.S.; Xiao, Z.; Suo, Y. A Possible Mechanism of Typhoon Effects on the Ionospheric F2 layer. *Chin. J. Space Sci.* **2006**, *26*, 92–97. [[CrossRef](#)]
7. Cai, J.T.; Zhao, G.Z.; Zhan, Y.; Tang, J.; Chen, X.B. The study on ionospheric disturbances during earthquakes. *Prog. Geophys.* **2007**, *22*, 695–701.
8. Parrot, M. DEMETER observations of manmade waves that propagate in the ionosphere. *Comptes Rendus Phys.* **2018**, *19*, 26–35. [[CrossRef](#)]
9. Zeren, Z. Electromagnetic Waves Induced by Strong Earthquakes and Non-Earthquake Sources in Geospace. Ph.D. Thesis, Beijing University of Aeronautics and Astronautics, Beijing, China, 2014.
10. Cao, J.; Yang, J.; Lu, L. Non-seismic induced electromagnetic waves in near-earth space. *Earthquakes* **2009**, *29*, 17–25. [[CrossRef](#)]
11. Parrot, M.; Benoist, D.; Berthelier, J.; Błęcki, J.; Chapuis, Y.; Colin, F.; Elie, F.; Fergeau, P.; Lagoutte, D.; Lefevvre, F. The magnetic field experiment IMSC and its data processing onboard DEMETER: Scientific objectives, description and first results. *Planet. Space Sci.* **2006**, *54*, 441–455. [[CrossRef](#)]
12. Lagoutte, D.; Brochot, J.Y.; Carvalho, D. DEMETER microsatellite scientific mission center data product description. *Demeter* **2006**.
13. Zhang, D.; Ying, C.; Wang, S. Research on imminent earthquake electromagnetic wave information. *China Earthq. Eng. J.* **1981**, *3*, 11–16.
14. Xu, W.; Tong, W.; Wu, P. Discussion on electromagnetic anomaly before earthquake. *Earthquake* **1982**, *1*, 24–26.
15. Lin, M.; Li, K. Impending earthquake electromagnetic wave anomaly. *J. Seismol. Res.* **1985**, 567–574.
16. Zhang, D.; Wang, S.; Zhang, N. Observational study on the precursor of impending earthquake electromagnetic wave. *Acta Seismol. Sin.* **1987**, 100–108+111.
17. Ouyang, X.-Y.; Wang, Y.-F.; Zhang, X.-M.; Wang, Y.-L.; Wu, Y.-Y. A New Analysis Method for Magnetic Disturbances Possibly Related to Earthquakes Observed by Satellites. *Remote Sens.* **2022**, *14*, 2709. [[CrossRef](#)]
18. Xiang, C.; Li, M.; Ma, Z.; Teng, C.; Li, Z.; Shao, Z. Ultra-Low Frequency Electromagnetic Emissions Registered during the 21 May 2021 Yangbi MS 6.4 Earthquake in China. *Nat. Sci.* **2022**, *14*, 1–12.
19. Ji, T.; Guo-Ze, Z.; Xiao-Bin, C.; Ji-Jun, W.; Yan, Z.; Qi-Bin, X. Introduction of payload for electro-magnetic emissions on seismic satellite. *Prog. Geophys.* **2007**, *22*, 679–686.
20. Xiong, P.; Long, C.; Zhou, H.; Battiston, R.; Zhang, X.; Shen, X. Identification of Electromagnetic Pre-Earthquake Perturbations from the DEMETER Data by Machine Learning. *Remote Sens.* **2020**, *12*, 3643. [[CrossRef](#)]
21. Otrakis, S.M.; Asano, T.; Hayakawa, M. Criticality analysis of the lower ionosphere perturbations prior to the 2016 Kumamoto (Japan) earthquakes as based on VLF electromagnetic wave propagation data observed at multiple stations. *Entropy* **2018**, *20*, 199. [[CrossRef](#)]

22. Wang, S.; Gu, X.; Luo, F.; Peng, R.; Chen, H.; Li, G.; Yuan, D. Observations and analyses of the sunrise effect for NWC VLF transmitter signals. *Chin. J. Geophys.* **2020**, *63*, 4300–4311.
23. Singh, V.; Hobara, Y. Simultaneous study of VLF/ULF anomalies associated with earthquakes in Japan. *Open J. Earthq. Res.* **2020**, *9*, 201–215. [[CrossRef](#)]
24. Zhao, G.Z.; Lu, J.X. Monitoring and analysis of earthquake phenomena by artificial SLF Waves. *Eng. Sci.* **2003**, *5*, 27–32.
25. Zhao, S.; Liao, L.; Zhang, X.; Shen, X. Full wave calculation of ground-based VLF radiation penetrating into the ionosphere. *Chin. J. Radio Sci.* **2016**, *31*, 825–833.
26. Loudet, L. SID Monitoring Station[EB/OL]. 2013. Available online: <https://sidstation.loudet.org/stations-list-en.shtml> (accessed on 18 June 2021).
27. He, Y.; Yang, D.; Chen, H.; Qian, J.; Zhu, R.; Parrot, M. SNR changes of VLF radio signals detected onboard the DEMETER satellite and their possible relationship to the Wenchuan earthquake. *Sci. China Ser. D* **2009**, *52*, 754–763. [[CrossRef](#)]
28. Molchanov, O.; Rozhnoi, A.; Solovieva, M.; Akentieva, O.; Berthelier, J.J.; Parrot, M.; Hayakawa, M. Global diagnostics of the ionospheric perturbations related to the seismic activity using the VLF radio signals collected on the DEMETER satellite. *Nat. Hazards Earth Syst. Sci.* **2006**, *6*, 745–753. [[CrossRef](#)]
29. Zhao, S.; Shen, X.; Zhima, Z.; Zhou, C. The very low-frequency transmitter radio wave anomalies related to the 2010 MS7.1 Yushu earthquake observed by the DEMETER satellite and the possible mechanism. *Ann. Geophys.* **2020**, *38*, 969–998. [[CrossRef](#)]
30. Muto, F.; Yoshida, M.; Horie, T.; Hayakawa, M.; Parrot, M.; Molchanov, O.A. Detection of ionospheric perturbations associated with Japanese earthquakes on the basis of reception of LF transmitter signals on the satellite DEMETER. *Nat. Hazards Earth Syst. Sci.* **2008**, *8*, 135–141. [[CrossRef](#)]
31. Zhang, X.; Zhao, S.; Song, R.; Zhai, D. The propagation features of LF radio waves at topside ionosphere and their variations possibly related to Wenchuan earthquake in 2008. *Adv. Space Res.* **2019**, *63*, 3536–3544. [[CrossRef](#)]
32. Shen, X.; Zhima, Z.; Zhao, S.; Qian, G.; Ye, Q.; Ruzhin, Y. VLF radio wave anomalies associated with the 2010 MS7.1 Yushu earthquake. *Adv. Space Res.* **2017**, *59*, 2636–2644. [[CrossRef](#)]
33. Rozhnoi, A.; Solovieva, M.; Parrot, M.; Hayakawa, M.; Biagi, P.F.; Schwingenschuh, K.; Fedun, V. VLF/LF signal studies of the ionospheric response to strong seismic activity in the Far Eastern region combining the DEMETER and ground-based observations. *J. Phys. Chem. Earth A/B/C* **2015**, *85–86*, 141–149. [[CrossRef](#)]
34. Slominska, E.; Blecki, J.; Parrot, M.; Slominski, J. Satellite study of VLF ground-based transmitter signals during seismic activity in Honshu Island. *Phys. Chem. Earth A/B/C* **2009**, *34*, 464–473. [[CrossRef](#)]
35. Solovieva, M.S.; Rozhnoi, A.A.; Molchanov, O.A. Variations in the parameters of VLF signals on the DEMETER satellite during the periods of seismic activity. *Geomag. Aeron.* **2009**, *49*, 532–541. [[CrossRef](#)]
36. Yang, M.; Huang, J.; Zhang, X.; Shen, X.; Wang, L.; Zeren, Z.; Qian, G.; Zhai, L. Analysis on dynamic background field of ionosphere ELF/VLF electric field in Northeast Asia. *Prog. Geophys.* **2018**, *33*, 2285–2294.
37. Huang, J.; Jia, J.; Yin, H.; Li, Z.; Li, J.; Shen, X.; Zhima, Z. Study of the Statistical Characteristics of Artificial Source Signals Based on the CSES. *Front. Earth Sci.* **2022**, *10*, 883836. [[CrossRef](#)]
38. Han, Y.; Wang, Q.; Huang, J.; Yuan, J.; Li, Z.; Wang, Y.; Liu, H.; Shen, X. Frequency Extraction of Global Constant Frequency Electromagnetic Disturbances from Electric Field VLF Data on CSES. *Remote Sens.* **2023**, *15*, 2057. [[CrossRef](#)]
39. Shen, X.; Zhang, X.; Yuan, S.; Wang, L.; Cao, J.; Huang, J.; Dai, J. The state-of-the-art of the China Seismo-Electromagnetic Satellite mission. *Sci. China Technol. Sci.* **2018**, *61*, 634–642. [[CrossRef](#)]
40. Hu, Y.; Zhima, Z.; Huang, J.; Zhao, S.; Guo, F.; Wang, Q.; Shen, X. Algorithms and implementation of wave vector analysis tool for the electromagnetic waves recorded by the CSES satellite. *Chin. J. Geophys.* **2020**, *63*, 1751–1765.
41. Wang, L.; Hu, Z.; Shen, X. Data processing methods and procedures of CSES satellite. *Natl. Remote Sens. Bull.* **2018**, *22*, 39–55. [[CrossRef](#)]
42. Zhou, B.; Yang, Y.; Zhang, Y.; Gou, X.; Cheng, B.; Wang, J.; Li, L. Magnetic field data processing methods of the China SeismoElectromagnetic Satellite. *Earth Planet. Phys.* **2018**, *2*, 455–461. [[CrossRef](#)]
43. Wang, X.; Cheng, W.; Yang, D.; Liu, D. Preliminary validation of in situ electron density measurements onboard CSES using observations from Swarm Satellites. *Adv. Space Res.* **2019**, *64*, 982–994. [[CrossRef](#)]
44. Yuan, G.; Zhu, X.; Huang, J. System design and key technology of electromagnetic monitoring and test satellite (Zhangheng-1). *J. Remote Sens.* **2018**, *22*, 32–38.
45. Han, Y.; Yuan, J.; Ouyang, Q.; Huang, J.; Li, Z.; Zhang, Y.; Wang, Y.; Shen, X.; Zeren, Z. Automatic Recognition of Constant-Frequency Electromagnetic Disturbances Observed by the Electric Field Detector on Board the CSES. *Atmosphere* **2023**, *14*, 290. [[CrossRef](#)]
46. Han, Y.; Yuan, J.; Feng, J.L.; Yang, D.; Huang, J.; Wang, Q.; Shen, X.; Zeren, Z. Automatic detection of horizontal electromagnetic wave disturbance in EFD data of Zh-1 based on horizontal convolution kernel. *Prog. Geophys.* **2022**, *37*, 11–18.
47. Zhang, R.; Zhang, J.; Yu, J. Frequency Offset Estimation in OFDM Systems Based on Signal Constellations. *Math. Probl. Eng.* **2015**, 1–9.
48. Gupta, A.K.; Naseer, E. A Study of Frequency Stability in Oscillators Due to Temperature Variations. *Int. J. Adv. Comput. Sci. Appl.* **2011**, *2*, 71–75.
49. Charles, P.; Francois, S. Aging of Atomic Oscillators: Fundamental Limits and Expectations. *Eur. Freq. Time Forum (EFTF)* **2016**, 305–310.

50. Matschek, N.; Zengerle, R.; von Stetten, F. Power Supply Considerations for Biomedical Implants. In Proceedings of the Annual International Conference of the IEEE Engineering in Medicine and Biology Society (EMBC), Buenos Aires, Argentina, 31 August–4 September 2010; pp. 1432–1436.
51. Murtaza, G.; Saad, S.M. Effect of Environmental Factors on the Performance of Local Oscillator in Analog TV Transmitter. In Proceedings of the 2015 IEEE 12th Malaysia International Conference on Communications (MICC), Kuching, Malaysia, 23–25 November 2015; pp. 102–105.
52. Xi, X.; Wang, H. Frequency Offset Effects on UWB Channel Estimation Performance. In Proceedings of the 2011 Asia-Pacific Conference on Communications, Sabah, Malaysia, 2–5 October 2011; pp. 806–810.
53. Madeiro, F.A.; Brito, R.A. Analysis of the Impact of Frequency Offsets in Underwater Acoustic OFDM Communications. In Proceedings of the 2016 IEEE 17th International Workshop on Signal Processing Advances in Wireless Communications (SPAWC), Edinburgh, UK, 3–6 July 2016; pp. 1–5.
54. Xu, M.; Wu, X. Effects of Frequency Offset on the Performance of Satellite Communication Systems. In Proceedings of the IEEE International Conference on Communication Technology (ICCT), Nanjing, China, 28–31 October 2020; pp. 258–262.
55. Gizatulin, A.V.; Tushin, A.O. Analysis of Signal Frequency Offset in Satellite Communication Systems. In Proceedings of the 2013 IEEE 33rd International Scientific Conference on Electronics and Nanotechnology (ELNANO), Kiev, Ukraine, 16–19 April 2013; pp. 564–567.
56. Li, J.; Meng, G.; You, X.; Zhang, R.; Shi, H.; Han, Y. Ionospheric Total Electron Content Disturbances Associated with Earthquakes from 1998 to 2015. *Surv. Geophys.* **2016**, *827–857*.
57. Liu, J.; Huang, R.; Wang, S.; Wei, W.; Qian, J. Precursory off-line disturbances of the earth's surface and the early time in tibetan plateau before Ms8. 1 Wenchuan earthquake. *Phys. Earth Planet. Inter.* **2013**, *224*, 37–44.
58. Tramutoli, V.; Castelli, D.; Pugliese, P.; Diolaiuti, E.; Balestrieri, R.; Viti, C.; Bordoni, L.; Pugliese, L. Satellite thermal infrared precursors of the 2009 L'Aquila earthquake. *Phys. Chem. Earth* **2012**, *66–74*.
59. Qian, J.; Zhu, W.; Zeng, M.; Wang, S.; Huang, Z.; Huang, R.; Liu, X.; Zhang, G.; Gao, Q. Ionospheric Anomalies before the 12 May 2008 Wenchuan Earthquake: Results from GPS Data in China. *J. Geophys. Res. Space Phys.* **2010**, *115*, A05305.
60. Ciralo, L.; Chienaldi, M.; Diebold, U.; Garofalo, F.; Grassi, P.; Gruppuso, A. A critical overview of electromagnetic waves for the detection of earthquakes. *IEEE Sens. J.* **2017**, *1373–1383*.
61. Chaudhary, G. Frequency Stability Analysis of Oscillators and its Techniques: A Review. *Int. J. Eng. Res. Technol.* **2019**, *12*, 1390–1394.
62. Kovacs, A.; Bakonyi, P. Temperature dependence of microwave circulator nonreciprocity. *IEEE Trans. Microw. Theory Tech.* **2013**, *61*, 2465–2477.
63. Daly, E.; Hilgers, A.; Glover, A. Space weather effects on satellites and forecasting the earth's space radiation environment. *Space Weather.* **2004**, *2*, 11.
64. Palhang, M.; Bornard, G. Assessment of Power Stability to Overcome High-Frequency Oscillations in Power Electronics. In Proceedings of the 2019 21st European Conference on Power Electronics and Applications (EPE'19 ECCE Europe), Genova, Italy, 2–5 September 2019; pp. 1–10.
65. Subbote, S.K.; Guermami, M.; Guo, H.; Celebi, H. Impact of environmental factors on the performance of organic photovoltaic systems in smart building applications. *Energy AI* **2018**, *2*, 100010.
66. Saravanakumar, R.; Shunmuganathan, K.L.; Rajasekar, K. An enhanced secured communication scheme using chaotic coupled kvik-based tms320c6713 processor. *Microprocess. Microsyst.* **2020**, *75*.
67. Truong, N.H.; Nguyen, H.M.; Nguyen, D.H.; Hong, S.P. A Digital Predistortion Technique for Flattening the Frequency Response in Nonlinear Power Amplifiers. *IEEE Trans. Circuits Syst. I Regul. Pap.* **2021**, *68*, 1572–1583.
68. Liu, Y.; Li, M.; Wang, X.; Zhang, Y.; Li, S. Privacy-Preserving Data Aggregation Scheme for Fog Computing in IoT. *Sensors* **2020**, *20*, 3891.
69. Akman, A.E.; Balli, E. Comparison of methods for estimating soil hydraulic properties on heavy clayey soils. *Comput. Geotech.* **2021**, *137*, 104210.
70. Radhakrishnan, R.; Singh, A.; Sarkar, S.P. Statistical and spectral analysis of ionospheric disturbances for wide-area GNSS augmentation systems. *Radio Sci.* **2017**, *52*, 940–955.
71. Wyss, M. Earthquake prediction: State-of-the-art and emerging methods. *Geosci. Front.* **2021**, *12*, 101–111.
72. Arvind, N. An unsupervised deep-learning framework for single-channel speech separation with improved deep clustering. *IEEE Trans. Audio Speech Lang. Process.* **2020**, *28*, 191–203.
73. Wakker, K. *Fundamentals of Astrodynamics*; Progress Publishers: Zubovsky Boulevard, Moscow, 1971.
74. Curtis, H.D. *Orbital Mechanics for Engineering Students*; Elsevier: Amsterdam, The Netherlands, 2013.
75. Pisacane, V.L. *Fundamentals of Space Systems*; Pisacane, V.L., Moore, R.C., Eds.; Oxford University Press: New York, NY, USA, 1994; 772p.
76. Chuvieco, E. *Fundamentals of Satellite Remote Sensing*; Taylor and Francis: Oxfordshire, UK, 2009.
77. Zhao, J.; Huang, Y. An Improved Method for Separating Ascending and Descending Orbits Based on Satellite Altimetry Data. *Remote Sens.* **2019**, *11*, 839. [[CrossRef](#)]
78. Jin, X.; Li, Z. Separation of Satellite Ascending and Descending Tracks in Swarm and Oersted Satellite Data. *J. Geod.* **2017**, *91*, 453–462.

79. Liu, T.; Zhang, L.; Liu, C.; Zhang, X.; Zhang, J. Satellite Orbit Segmentation and Analysis Based on High-Density Clustering. *Sensors* **2020**, *20*, 2234. [[CrossRef](#)]
80. Victoria, M.; Lopez, J.; Sanz, R.; Garcia-Fernandez, M. Spectral Analysis of Orbital Changes in GNSS Satellites for Improving Orbit Prediction. *Navigation. J. Inst. Navig.* **2016**, *63*, 447–460. [[CrossRef](#)]

Disclaimer/Publisher’s Note: The statements, opinions and data contained in all publications are solely those of the individual author(s) and contributor(s) and not of MDPI and/or the editor(s). MDPI and/or the editor(s) disclaim responsibility for any injury to people or property resulting from any ideas, methods, instructions or products referred to in the content.